npj | computational materials

Article

Published in partnership with the Shanghai Institute of Ceramics of the Chinese Academy of Sciences

https://doi.org/10.1038/s41524-024-01325-3

Unraveling active sites regulation and temperature-dependent thermodynamic mechanism in photothermocatalytic CO_2 conversion with H_2O

Li Zhang, Changqi Li, Yan Liu, Chenyu Xu & Yanwei Zhang

In the photothermal synergistic catalytic conversion of CO_2 and H_2O, the catalyst harnesses solar energy to accumulate heat, thereby elevating the reaction system's temperature. The influence of this temperature effect on surface chemical reactions remains an underexplored area. Here the impact of temperature on the surface-level thermodynamic reactions and conversion of CO_2 with H_2O on oxide semiconductors at the atomic scale was investigated using first-principle calculations. 13 different metal oxides and 5 transition metal clusters were used to introduce surface functional sites on the TiO_2 supporting catalyst. The potential metal oxide cocatalysts that could be most beneficial to the following conversion of CO_2 by H_2O were initially screened by calculating the degrees of promotion of CO_2 adsorption and activation of surface H to provide protons. The proton donation and hydrogen evolution difficulty from H_2O were further analyzed, identifying transition metal cocatalysts that promote direct CO_2 hydrogenation. Upon introducing bifunctional sites to facilitate adsorption and reduction, the production of CH_3OH and CH_4 could be further enhanced through the facilitation of the proton donation process of H_2O. The results of Gibbs free-energy calculations revealed that increasing temperature enhances the reaction thermodynamics for each C1 product formation at different surface sites to varying degrees. These findings offer valuable theoretical insights for designing and regulating active sites on oxide semiconductor surfaces for efficient photothermal catalytic CO_2 reduction by H_2O.

Increasing apprehensions concerning global energy demand and greenhouse impacts have fueled the advancement of clean and renewable energy systems. The utilization of solar energy for instigating chemical reactions to convert CO_2 into solar fuels is considered a potential solution, which can simultaneously mitigate the greenhouse effect and ameliorate the energy crisis[1,2]. Photothermal synergistic catalytic conversion of CO_2 with H_2O, when viewed from a catalytic pathway perspective, amalgamates the benefits of photogenerated carrier-driven photocatalysis and temperature-driven traditional thermal catalysis, and enables the coupling of non-thermal and thermal effects of solar radiation[3]. In terms of the feedstock, the abundance and environmental friendliness of hydrogen as a source make this approach exceptionally promising, and the development in this field is rapidly advancing[4,5]. In the process of advancing studies on CO_2 photothermal conversion, it is imperative to understand the separate roles of light and heat and, subsequently, grasp the synergistic mechanism. Directly elucidating photothermal synergy and systematically assessing the combined effects of light and heat excitation on catalytic conversion has always been a challenging and complex issue[6].

Several recent reviews have presented varying definitions for the terminology concerning the impacts of light and heat[7–12], signifying a growing trend in research that seeks to elucidate these effects from a fundamental mechanistic standpoint. The photothermal process is jointly contributed by photochemistry and thermochemical mechanistic pathways. Accordingly, Mateo et al.[7] categorized it as "hot-carrier" and "thermal" effects, while Song et al.[8] referred to it as "light" and "thermal" effects. The more general term, "light" and "heat", are commonly encountered in current research literature[9,10]. Ozin introduced the concepts of "photochemical" and "photophysical" effects[6], and highlighted the ongoing challenge of determining the relative contributions of these two effects to reaction rate and selectivity. Becker et al.[11] adopted a simplified model for evaluating the

State Key Laboratory of Clean Energy Utilization, Zhejiang University, Hangzhou 310027, China. e-mail: mrxcy@zju.edu.cn; zhangyw@zju.edu.cn

"photochemical" and "thermochemical" effects in the context of exothermic reactions involving solid catalysts exposed to irradiation. Fang et al.'s review focused on the synergistic effects of "thermal and photo energies" in catalysis[12]. Chen et al.[13] have unveiled the synergistic mechanism involving the coupling of "photo" and "photothermal" effects with specific catalysts like Ru@$Ni_2V_2O_7$. It should be noted that the temperature effects mentioned here collectively refer to the increase in system temperature after the accumulation of thermal energy caused by thermal effects, which may be attributed to the non-radiative relaxation of semiconductors, localized heating induced by plasma, and thermal vibration of molecules[14]. This is relative to the non-thermal effects involving the generation and utilization of high-energy carriers[15]. The elevation in reaction temperature will significantly influence the entire reaction system, encompassing reaction thermodynamics and kinetics, product selectivity and yield, thermal active sites, and catalyst structure[9,12]. Some recent studies have identified the temperature effects including enhancements in diffusion rates, adsorption-desorption processes, charge carrier migration, and chemical reactions[16–18]. Temperature also facilitates the surmounting of activation energy barriers[19], activation of thermally active sites[20], and adjustments to the redox potential of half-reactions[21,22], along with alterations in catalyst band gaps[23]. Nevertheless, there remains a lack of atomic-level understanding of the intricate surface chemistry and the thermodynamic reaction path mechanism affected by temperature in the CO_2 catalytic reduction process[24,25].

While trying to break through research on the mechanisms underlying both non-thermal and thermal effects, scholars turn their eyes toward the target reaction of CO_2 conversion with H_2O, a pivotal and fundamental reaction in the field of solar energy conversion. It is well-known that the chemical properties of CO_2 and H_2O are notably stable, necessitating materials characterized by favorable non-thermal effects to surmount the stringent reaction conditions required for the activation of reactant molecules. Numerous conventional metal oxide semiconductors, including TiO_2, have been utilized for photothermal CO_2 reduction in the presence of pure H_2O. However, the majority of the reported systems thus far have demonstrated relatively low CO_2 conversion rates, typically in the magnitude of $\mu mol \cdot g^{-1} \cdot h^{-1}$ [26,27]. Based on the basic principles and processes of photothermal catalytic CO_2 reduction by H_2O, ongoing research efforts on improving CO_2 conversion performance mainly focus on strengthening the following three key steps: 1. Photon absorption; 2. Photogenerated carrier separation; 3. Surface catalytic reactions involving CO_2 and H_2O (including adsorption of reactants, and desorption and reduction of intermediates, etc.)[28]. For the third step, multiple active sites need to be designed on the catalyst surface to simultaneously achieve CO_2 reduction and H_2O dissociation, which still remains tremendously challenging[29]. In the photothermal catalytic reaction system where CO_2 and H_2O coexist, either H_2O or H_2 might become proton sources. There are three situations in which CO_2 reduction occurs. One is that H_2O first undergoes photooxidation (assisted by photogenerated holes) to produce protons, the second is that H_2O directly provides protons, and the third is that photogenerated holes also assist H_2 dissociation producing protons. Then protons reduce CO_2 with photogenerated electrons. While the process of H_2O splitting for hydrogen evolution can supply H^+ to reduce CO_2, it simultaneously competes with conduction band electrons for CO_2 reduction, diminishing the effective reduction of CO_2 by photoexcited electrons[30]. Additionally, H_2O tends to have a higher propensity for surface adsorption on photocatalysts due to its high polarity. In contrast, initial adsorption and activation of CO_2 usually require a huge potential barrier. These result in low CO_2 reduction efficiency and poor hydrocarbon product selectivity[31,32]. Surface defect engineering[33] and co-catalyst engineering[34] have important applications in photothermal catalytic CO_2 reduction reactions[35]. In addition to bringing about alterations in the band gap and electronic structure, thereby changing the radiation absorption and conversion performance of the material, the introduction of oxygen vacancies can also function as reaction active sites for the adsorption and activation of surface species during the catalytic process[36,37]. Similarly, the incorporation of metal oxides and the loading of nanometal particles can further create tailored functional sites on the material surface, enhancing the selective adsorption and activation of reactants and facilitating the subsequent reduction of key intermediates[38,39]. Both approaches have been proven to be powerful means to improve the performance of CO_2 reduction by pure H_2O on the surface of oxide semiconductors[40]. Alkaline-earth metal oxides including MgO, CaO, SrO, BaO[41,42], as well as rare-earth metal oxides such as La_2O_3, CeO_2, Pr_6O_{11}[43–45] have been widely used as adsorption cocatalysts to introduce basic active sites on the surface of support oxides. Other metal oxides like Al_2O_3[46], Ga_2O_3[47], ZrO_2[48], Ta_2O_5[49], HfO_2[50], and WO_3[51] have also been experimentally explored for their potential in photocatalytic reduction of CO_2 and H_2O, which show promise as promoters to enhance catalytic activity by enriching surface-active sites or modifying the electronic structure. Additionally, Mn, Fe, Co, Ni, and Cu are relatively low-cost representative transition metals capable of activating CO_2 and H_2[52–54].

This work aims to reveal the effect of temperature on the surface reaction path mechanism coupling CO_2 reduction and H_2O decomposition involving multiple surface intermediates and hydrodeoxygenation steps. Anatase TiO_2 ($aTiO_2$) served as the supporting catalyst, and successive modifications were made on its surface using 13 different metal oxides (La_2O_3, Al_2O_3, Ga_2O_3, CaO, MgO, SrO, CeO_2, HfO_2, ZrO_2, BaO, Ta_2O_5, Pr_6O_{11}, WO_3) and 5 transition metal (Mn, Fe, Co, Ni, and Cu) clusters. Subsequently, the adsorption and conversion processes of CO_2 and H_2O at the distinct surface adsorption and reduction sites correspondingly introduced through these modifications were studied. It was found that pure Ti-O-M sites can promote CO_2 adsorption, but do not necessarily facilitate subsequent reduction reactions. The metal oxide cocatalysts that may be most beneficial to the following conversion of CO_2 were initially screened as La_2O_3, Al_2O_3, and Ga_2O_3, which can not only promote CO_2 adsorption but also activate surface H to provide protons. Subsequent loading of Co_4 and Ni_4 transition metal clusters further promoted the proton-donating process of H_2O splitting while inhibiting hydrogen evolution, and are expected to improve the CH_3OH and CH_4 selectivity by further promoting the direct hydrogenation of CO_2. In addition, the results of Gibbs free-energy calculations indicate that increasing temperature enhances the thermodynamics of C1 product formation on the surface at different sites to varying degrees.

Results and discussion

The CO_2 photoreduction with H_2O on the surface of metal oxide semiconductor involves sophisticated multi-reaction paths, accompanied by multiple proton-coupled electrons transfer[55], and protonation, deoxygenation, and hydroxylation steps. It results in a variety of intermediate species and a complex reaction process. The elaborated thermodynamic reaction network of CO_2 conversion with H_2O on $aTiO_2$(101)-based surface has been reported in our previous work[56]. To observe its temperature-dependent characteristics, here the reaction paths of CO_2 with H_2O to C_1 products (mainly CO, CH_3OH and CH_4) on pure $aTiO_2$(101) surface at 100~400 °C were calculated, and the energy barriers comparison of all intermediate steps were shown in Supplementary Fig. 3a. During the process of photothermal catalytic CO_2 conversion with H_2O, both H_2O and H_2 might provide proton sources and reduce CO_2 together with photogenerated electrons. Here we focused on the forward protonation steps of CO_2 conversion (as shown in Fig. 1). It was found that, on pure $aTiO_2$(101) surface, the energy barriers of certain intermediate steps exhibited an increase as temperature ascends, while others displayed a decrease. However, the fundamental trajectory of the reaction remained unaffected by changes in temperature. The rate-determining step (RDS) of producing CO, CH_3OH, and CH_4 was always the CO_2 adsorption step but with its energy barrier increased from 0.41 eV to 1.04 eV (as shown in Supplementary Fig. 3b), which might be attributed to the fact that the adsorption is exothermic commonly while the increasing temperature would inhibit the reactants adsorption. Therefore, it means that reactant adsorption under high-temperature conditions plays a critical role in the whole reaction. Optimizing surface adsorption sites will be considered first. Furthermore, the subsequent conversion of reactants on the catalyst also exhibited a strong correlation with the presence of active sites on the surface. Basically,

introducing adsorption sites and reduction sites on the support semiconductors has been regarded as an effective approach to enhance the performance of photothermal catalytic CO_2 reduction[57]. In this context, the discussion revolves around elucidating the mechanism that governed the influence of temperature on the thermodynamic reaction process path (including the adsorption and conversion of reactants and intermediates) and product selectivity during the photothermal catalysis of CO_2 conversion with H_2O on semiconductor surfaces featuring functional active sites.

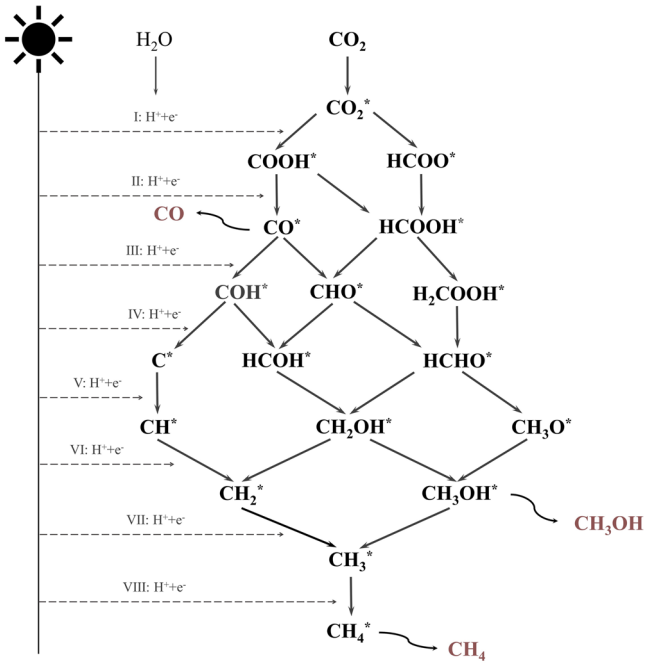

Fig. 1 | The protonation steps and reaction network of CO_2 conversion with H_2O to C_1 products. During the photothermal catalytic CO_2 conversion with H_2O, light irradiates H_2O molecules to split and provide protons and electrons to reduce CO_2. It takes two protons and two electrons to generate CO, six protons and two electrons to generate CH_3OH, and eight protons and two electrons to generate CH_4.

Adsorption and activation of CO_2, H_2O, and H atom

The pure aTiO_2(101) surface owns relatively simple reaction sites for reactant adsorption and activation. For the purpose of designing and providing selective sites for the adsorption of CO_2, H_2O, and H, 13 types of M_xO_y (La_2O_3, Al_2O_3, Ga_2O_3, CaO, MgO, SrO, CeO_2, HfO_2, ZrO_2, BaO, Ta_2O_5, Pr_6O_{11}, WO_3) were decorated on the pure aTiO_2(101) surface. As demonstrated in Fig. 2a, the energy barriers for adsorption and activation of CO_2 and H_2O molecule, H atom on surface Ti-O (V_O)-M sites were calculated. It can be concluded that both photoinduced V_O and doped M_xO_y promoted CO_2 adsorption to varying extents. Compared with this, H_2O adsorption was slightly affected, which emphasized the favorable effects of surface oxygen defects and basic sites on promoting the initial activation and selective adsorption of CO_2. Regarding the adsorption of H atoms, La_2O_3, Al_2O_3, and Ga_2O_3 doping exerted the most significant influence among all modified metal oxides. On the Ti-O-M (M=La, Al, Ga) site, the adsorption energy of H attained a notably diminished value. The charge density difference analysis was conducted for H adsorption on M_xO_y-decorated surfaces. As depicted in Supplementary Fig. 4, the electron gains and losses between the H atom and the surface were notably pronounced on surfaces doped with La_2O_3, Al_2O_3, and Ga_2O_3, with an increased charge transfer observed. A higher level of activation of H on the surface could potentially enhance the favorability of CO_2 hydrogenation. It should be noted that the difficulty in creating oxygen vacancies on the surface post-doping with distinct oxides exhibited differing degrees, and the calculated oxygen vacancy formation energy was presented in Fig. 2b for reference. Broadly speaking, when the valence state of the doped oxide's metal cations $M^{2y/x+}$ increased, detaching surface oxygen became more difficult, which might be attributed to the more pronounced charge compensation effect stemming from low-valent metal cations[58]. On surfaces doped with CaO, MgO, SrO, and BaO, the formation energy of V_O experienced a significant reduction, leading to the ease of forming Ti-Vo-M sites. This made reactant molecules and atoms exhibit a propensity for adsorption and activation directly on the defective surface. Comparatively, the presence of photoinduced V_O and the introduction of La_2O_3, Al_2O_3, and Ga_2O_3 on the aTiO_2 surface demonstrated a relatively potent promotional effect on CO_2 activation. Additionally, during photothermal catalysis reactions, light irradiation triggered the generation of oxygen vacancies on the material's surface. Under these circumstances, the adsorption energy of CO_2 on the surface of La_2O_3, Al_2O_3, and Ga_2O_3-doped TiO_2 was indicated in Supplementary Table 1. Notably, the adsorption energy of CO_2 evolved from −1.20 eV, −0.77 eV, and −0.76 eV (in the absence of surface defects) to −0.61 eV, −0.52 eV, and

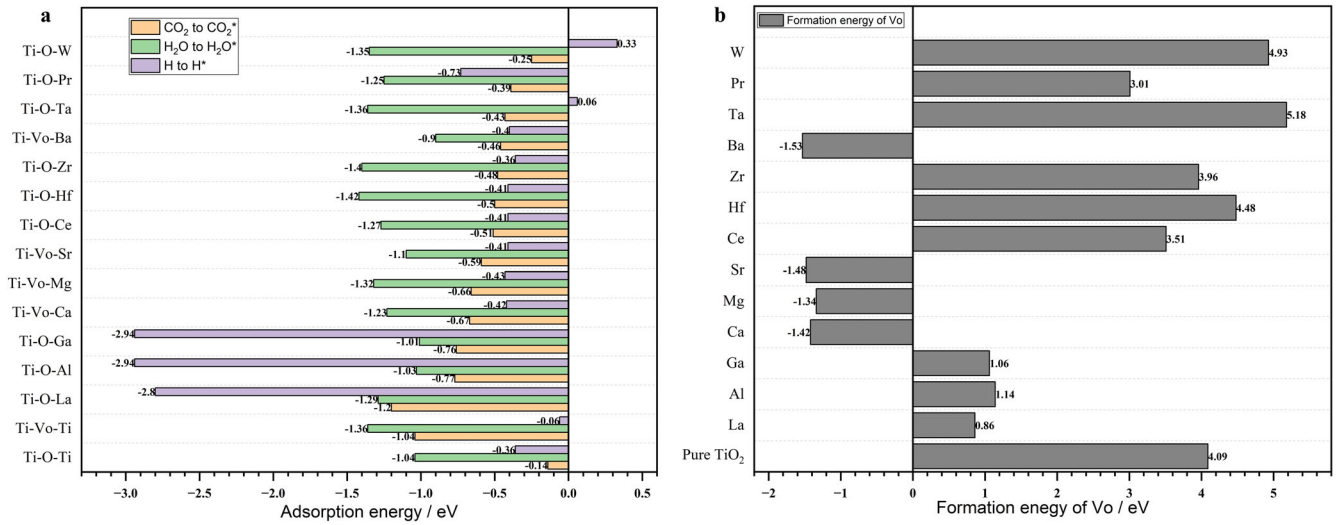

Fig. 2 | Comparison of the difficulty of adsorbing and activating CO_2, H_2O molecules, H atom, and forming V_O on TiO_2 surfaces before and after M_xO_y decorating. a Energy barriers (E_{ads}) for activating CO_2, H_2O molecules, and H atoms to CO_2^*, H_2O^*, and H^*, respectively, on different surface sites. **b** Formation energy of V_O on corresponding surfaces.

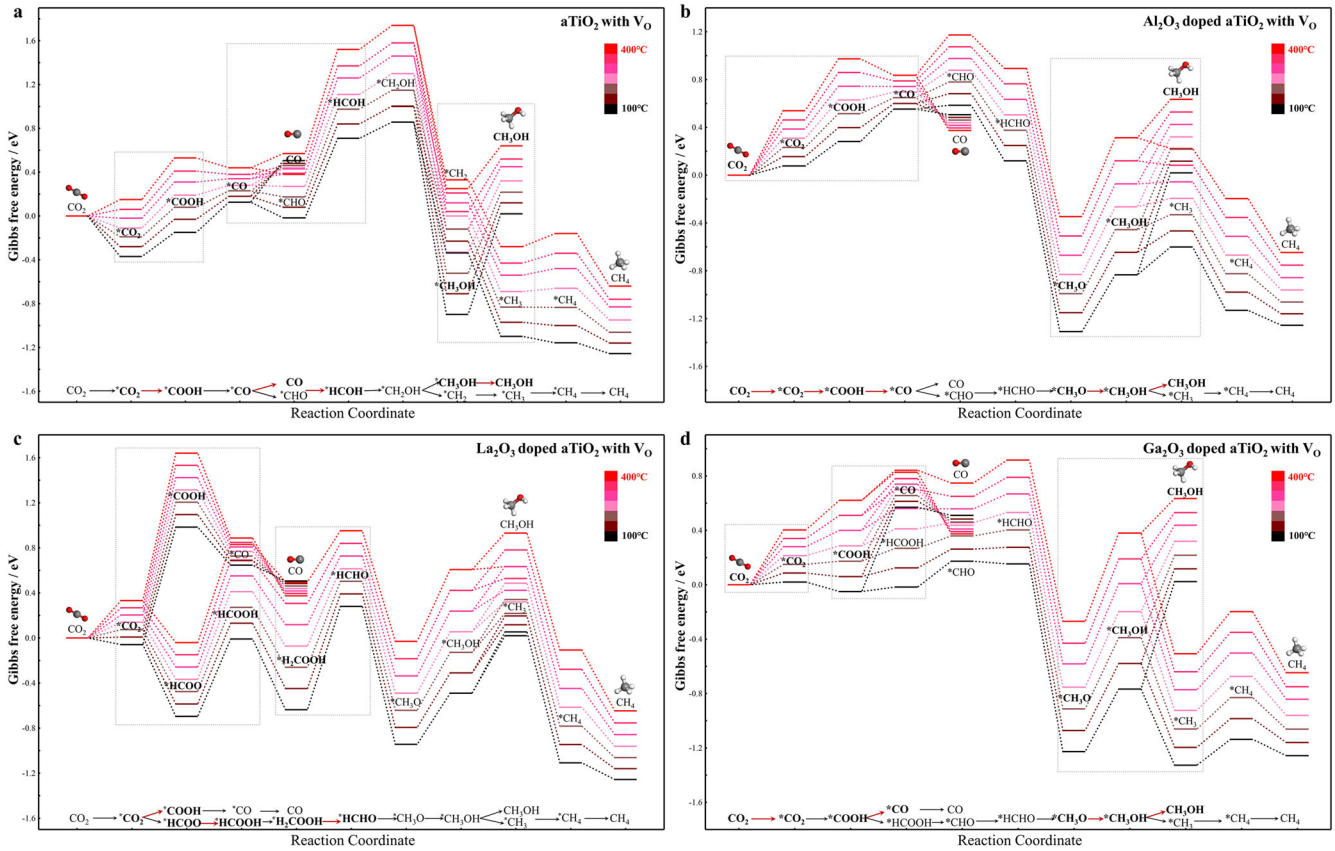

Fig. 3 | Reaction free-energy profiles of thermodynamic reaction pathways for multi-electron conversion of CO_2 to C_1 (CO, CH_3OH, and CH_4) products at varying temperatures (100~400 °C). Different reaction pathways and key intermediate steps are experienced on the surfaces of **a** $aTiO_2$ with V_O, **b** Al_2O_3-doped $aTiO_2$ with V_O, **c** La_2O_3-doped $aTiO_2$ with V_O, and **d** Ga_2O_3-doped $aTiO_2$ with V_O that strengthen the adsorption of reactants.

−0.52 eV respectively, signifying an increase yet maintaining a promotional effect. The enhancement of the basic sites introduced via doping for subsequent CO_2 conversion reactions relied on the availability of protons and electrons. The collaborative presence of synergistic surface oxygen defects and basic sites worked in tandem to amplify the reaction's thermodynamics, facilitating the multi-electron conversion of CO_2 to yield C1 products[56]. Based on the efficacy of La_2O_3, Al_2O_3, and Ga_2O_3 in augmenting the adsorption and activation of CO_2 molecules and H atoms, comprehensive calculations of the entire thermodynamic reaction paths for photothermal catalytic CO_2 conversion to C_1 products (CO, CH_3OH, and CH_4) at varying temperatures were performed on the respective defective surfaces doped with these compounds.

Temperature influence on the thermodynamic path of surface CO_2 conversion via enhanced adsorption sites

Thermodynamically, adsorption is exothermic, with a typically negative temperature impact. In other words, as the temperature increases, the strength of adsorption decreases. Yet, when examining surface CO_2 conversion reactions that encompass various intermediate steps, the interplay between temperature and these reactions becomes notably intricate compared to the simpler phenomenon of adsorption. On the surface-active sites that strengthen the adsorption of reactants, the reaction pathways of CO_2 conversion to CO, CH_3OH, and CH_4 at varying temperatures were illustrated in Figs. 3 and 4. As shown in Figs. 3a and 4a, on the defective $aTiO_2$ surface, the RDS of each product was different from that on the pure $aTiO_2$ surface. In the process of CO generation through '$CO_2 \rightarrow {}^*CO_2 \rightarrow {}^*COOH \rightarrow {}^*CO \rightarrow CO$', CO_2 adsorption was no longer the RDS on the defective surface. Instead, the RDS could involve either CO desorption or protonation of ${}^*CO_2$ to form ${}^*COOH$. With a temperature increased from 100 °C to 150 °C, CO desorption became the dominant RDS for CO production, resulting in a reduction of the associated energy barrier (from 0.49 eV to 0.31 eV). However, upon further elevation to 200 °C, the RDS transitioned to '${}^*CO_2$ protonation to ${}^*COOH$', accompanied by an energy barrier increase (from 0.27 eV to 0.38 eV) as temperature rose. Similarly, the RDS for CH_3OH production underwent alterations (from '${}^*CH_3OH \rightarrow CH_3OH$' to '${}^*CHO \rightarrow {}^*HCOH$'), and the energy barrier first decreased and then increased. This suggested the existence of an optimal thermodynamic temperature range for CO and CH_3OH generation, specifically between 150 °C and 200 °C. Meanwhile, the energy barrier associated with the RDS (${}^*CHO \rightarrow {}^*HCOH$) for CH_4 production showed an upward trend with increasing temperature, eventually being consistent with the energy barrier observed for CH_3OH production.

Across defective surfaces featuring various introduced basic sites, the reaction paths of C1 products exhibited discrepancies. Different surfaces tended to favor distinct optimal reaction paths, and engaged diverse reaction intermediates, as presented in Supplementary Fig. 5. When the temperature increased, notable on the Al_2O_3 doped surface as shown in Figs. 3b and 4b, the RDS for CO production experienced a sequential transformation: transitioning from '${}^*COOH \rightarrow {}^*CO$' to '${}^*CO_2 \rightarrow {}^*COOH$', and finally culminating in CO_2 adsorption. This sequential evolution was accompanied by an initial reduction followed by an eventual increase in the associated energy barrier. Notably, a thermodynamically favorable temperature range for CO production emerged, peaking around 150 °C. Likewise, for CH_3OH production, the RDS shifted from '${}^*CH_3OH \rightarrow CH_3OH$' to '${}^*CH_3O \rightarrow {}^*CH_3OH$' with increasing temperature, leading to an initial energy barrier decrease followed by an increase. The most thermodynamically favorable temperature for CH_3OH production was approximately 250 °C. Conversely, the energy barrier for the RDS of CH_4 production (${}^*CH_3O \rightarrow {}^*CH_3OH$) increased consistently with temperature. On the La_2O_3 doped surface as shown in Figs. 3c and 4c, the RDS of CO production was always '${}^*CO_2$

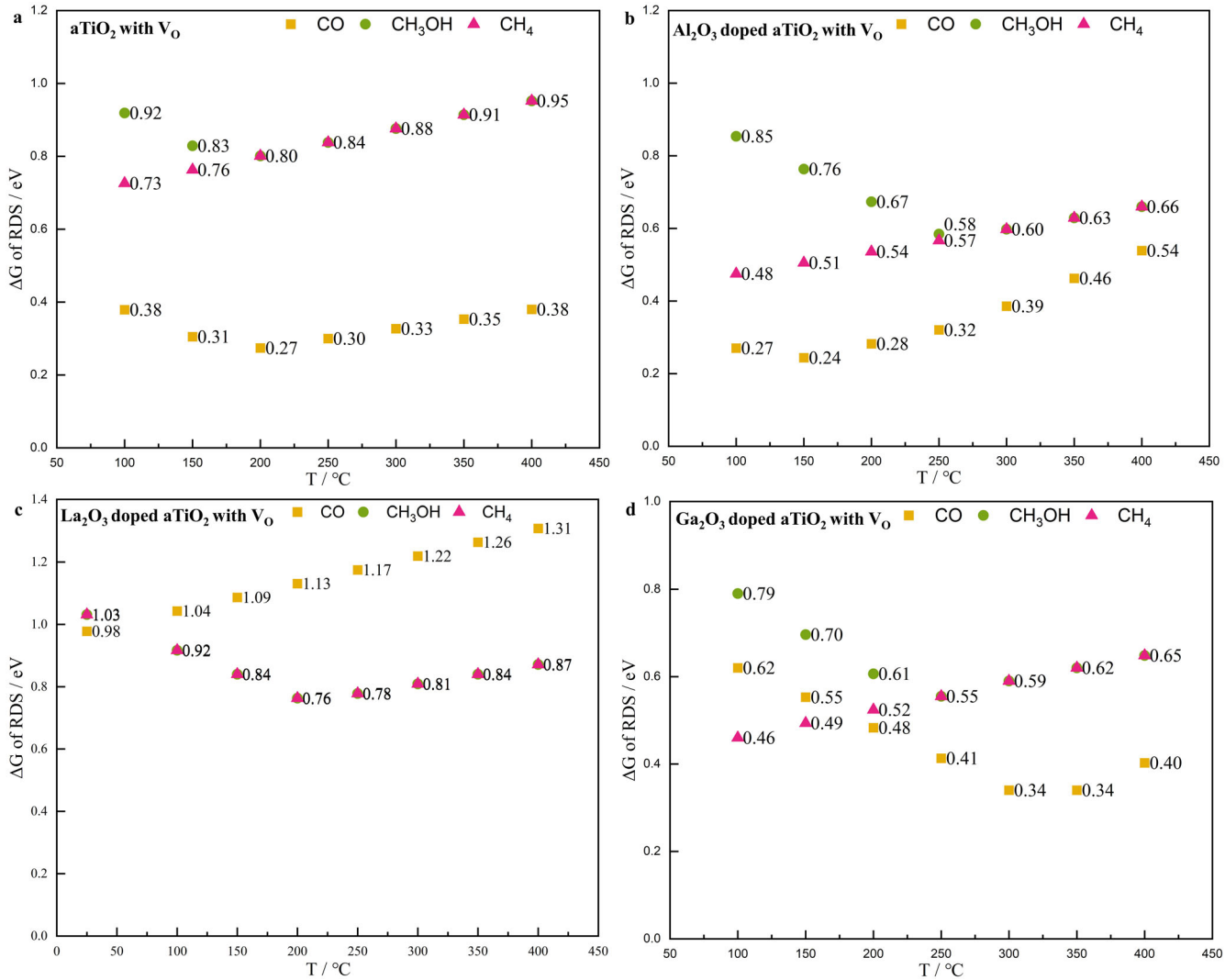

Fig. 4 | Comparison of temperature-dependent alterations in the RDS energy barriers for CO, CH_3OH, and CH_4 production. The Gibbs free-energy change of RDS under the temperature range of 100~400 °C on the surface of **a** $aTiO_2$ with V_O, **b** Al_2O_3-doped $aTiO_2$ with V_O, **c** La_2O_3-doped $aTiO_2$ with V_O, and **d** Ga_2O_3-doped $aTiO_2$ with V_O, respectively.

protonation to *COOH' as the temperature rose, but the energy barrier continued to increase (from 0.98 eV at 100 °C to 1.31 eV at 400 °C), which was not conducive to the formation of CO. The RDS for CH_3OH and CH_4 production decreased first and then increased. In the temperature range from 100 °C to 200 °C, the pivotal step was the conversion of $^*H_2COOH$ to *HCHO, and the energy barrier declined with rising temperature, reaching its minimum value of 0.76 eV at 200 °C. Subsequently, as the temperature continued to rise, the RDS transitioned to '*HCOO→*HCOOH', suggesting that the most thermodynamically favorable temperature for CH_3OH and CH_4 production might be approximately 200 °C. In addition, the thermodynamic tendency of the C_1 products evolved with increasing temperature, distinct from both undoped and Al_2O_3-doped surfaces. As shown in Fig. 4c, at lower temperatures (approximately lower than 50 °C), the energy barrier for CO production was the lowest, suggesting a thermodynamic preference for CO generation at this time. While as the temperature rose, the RDS energy barrier for CO production increased until it surpassed that for CH_3OH and CH_4 production, and remained high thereafter, leading to increased selectivity for CH_3OH and CH_4. With Ga_2O_3 doping, as shown in Figs. 3d and 4d, an increase in temperature results in a rising energy barrier for the RDS ('$^*CH_3O$→$^*CH_3OH$') of CH_4 production. The RDS for CH_3OH production transitioned from CH_3OH desorption to '$^*CH_3O$ conversion to $^*CH_3OH$', with its energy barrier displaying an initial decrease followed by an increase. A similar trend was observed for the RDS governing CO production. This transition involved a shift from '*COOH→*CO' to CO_2 adsorption as the temperature escalated. Furthermore, at temperatures below about 175 °C, the RDS energy barrier for CH_4 production was lower than that for CO and CH_3OH. However, as the temperature exceeded 175 °C, the energy barrier for CO production decreased below that for CH_3OH and CH_4, signifying that this increasing temperature enhanced the thermodynamic inclination toward CO production.

It can be seen from the above that surface doping with basic metal oxides notably influenced the reaction path for CO_2 reduction to C_1 products by altering the reaction intermediates and key steps. The energy barriers of the rate-determining steps for the formation of C1 products corresponding to the different adsorption-assisting active sites introduced changed and were affected by temperature. The higher temperature accentuated the thermodynamic favorability of multi-electron conversion of CO_2 into C_1 products. The temperature variation resulted in shifts in the relative ease of producing CO, CH_3OH, and CH_4, as shown in Supplementary Fig. 6. To elaborate, at lower temperatures, the RDS energy barrier for CO production was the lowest on Al-V_O-Ti site, while the RDS energy barriers for CH_3OH and CH_4 production were the lowest on pure Ti-O-Ti site, which are lower than those of all defective and doped surfaces. Before 250 °C, it was difficult to produce C1 on La-V_O-Ti, with the energy barrier

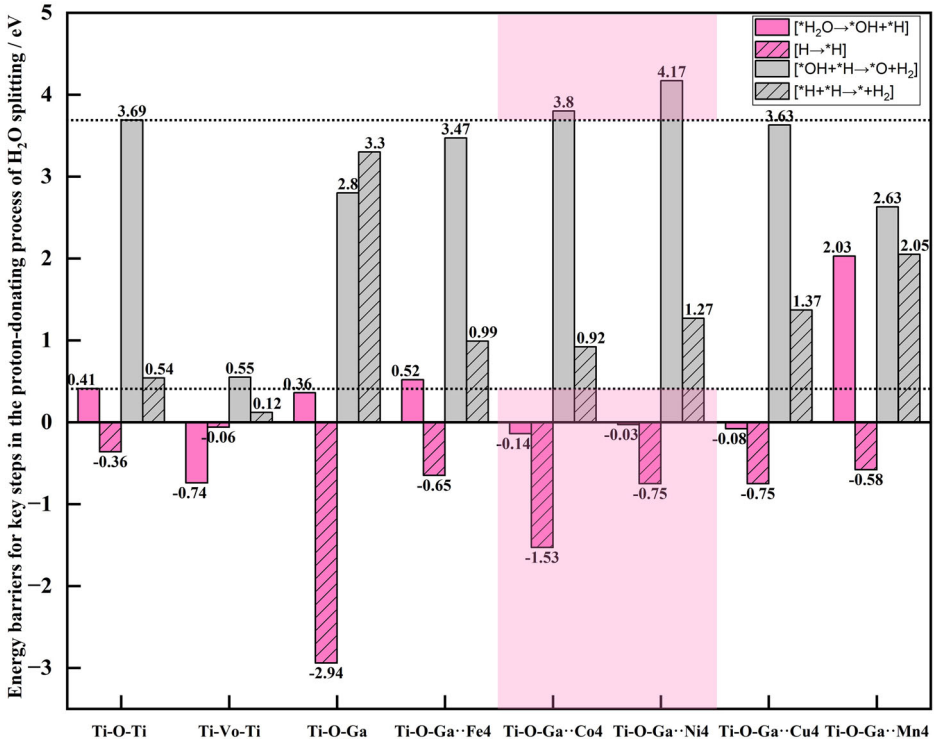

Fig. 5 | Analysis of energy barriers for key steps ($^*H_2O \rightarrow {}^*OH + {}^*H$, $H \rightarrow {}^*H$, $^*OH + {}^*H \rightarrow {}^*O + H_2$, and $^*H + {}^*H \rightarrow {}^* + H_2$) in the proton-donating process of H_2O splitting on different surface-active sites. The upper dotted line of the figure is aligned with the energy barrier of the hydrogen evolution step ($^*OH + {}^*H \rightarrow {}^*O + H_2$) at the pure Ti-O-Ti site, and the dotted line below is aligned with the energy barrier of the water-splitting adsorption step ($^*H_2O \rightarrow {}^*OH + {}^*H$) at the pure Ti-O-Ti site. The surface site where the pink rectangular area is located represents which has the potential to promote water splitting to generate $^*H$ and activate H while inhibiting the formation of H_2.

for CO exceeding that of CH_3OH and CH_4 and higher than that on Ti-O-Ti site. However, as the temperature rose, Ti-V_O-Ti site exhibited the lowest RDS energy barrier for CO production, while Ga-Vo-Ti site exhibited the lowest RDS energy barrier for CH_3OH and CH_4 production, maintaining this status at higher temperatures. The RDS energy barrier for CO production on La-V_O-Ti remained high, but CH_3OH and CH_4 production was enhanced. Although the temperature did not alter the overall reaction path, it did impact the selectivity of each surface C_1 product by modifying the rate-determining steps and energy barriers associated with each C_1 product. Elevated temperatures might promote CO selectivity (with Ga_2O_3 doping) and CH_3OH/CH_4 selectivity (with La_2O_3 doping).

Temperature influence on CO_2 conversion with H_2O at bifunctional sites via further loading transition metal clusters

During the photothermal catalytic reaction, the photoinduced oxygen vacancies on the surface of the oxide semiconductor were likely to be occupied in the intermediate steps of CO_2 conversion (especially in the deoxygenation step), which encompass the following steps: 'V_O-$^*CO_2 \rightarrow {}^*CO$', '$V_O$-$^*COOH \rightarrow {}^*COH$', '$V_O$-$^*HCOO \rightarrow {}^*CHO$', '$V_O$-$^*HCOOH \rightarrow {}^*HCOH$', '$V_O$-$^*HCOO \rightarrow {}^*CHO$', '$V_O$-$^*CO \rightarrow {}^*C$', '$V_O$-$^*CHO \rightarrow {}^*CH$', '$V_O$-$^*HCHO \rightarrow {}^*CH_2$', and '$V_O$-$^*CH_3O \rightarrow {}^*CH_3$'. Once the oxygen vacancies were consumed, the doped metal oxide was not conducive to the reduction reaction. As shown in Supplementary Fig. 7, it was calculated that at the M-V_O-Ti (M=Al, La, Ga) site, oxygen vacancies were more prone to being occupied by intermediate species $^*HCOOH$, $^*CO_2$, and $^*CO_2$ respectively to yield $^*HCOH$, $^*CO$, and $^*CO$. Subsequently, $^*HCOH$ and $^*CO$ underwent protonation. However, the energy barrier for the subsequent steps, specifically from $^*CH_2OH$ to form $^*CH_3OH$ or from $^*CH_3$ to form $^*CH_4$, was exceedingly high. Consequently, the production of CH_3OH and CH_4 becomes exceptionally challenging at this stage, underscoring the need for further enhancement of the reduction of key intermediates. This also showed that the introduction of adsorption-assisted sites primarily facilitates reactant adsorption, without necessarily guaranteeing the promotion of subsequent reduction reactions.

It was generally believed that transition metal clusters can activate H_2 to $^*H$[52], or promote the H_2O dissociation[59], thereby providing $^*H$ to facilitate the direct hydrogenation of CO_2. But at the same time, they might also catalyze the hydrogen evolution of H_2O[60,61], which engendered competition with hydrocarbon products during the reduction of CO_2 by H_2O. Various transition metal clusters were further loaded onto Ga_2O_3-doped TiO_2 surface, to delve deeper into the conversion of CO_2 with H_2O into hydrocarbon products by introducing dual sites that assist in adsorption and reduction. In metal oxide semiconductor systems, the hydrogen evolution step was often identified as the rate-determining stage in the decomposition of H_2O on the surface[62,63]. It was considered that a higher energy barrier for the hydrogen evolution step signifies effective suppression of competitive hydrogen evolution. The proton-donating process of water splitting was calculated on the surfaces supported by a series of transition metal clusters (Mn, Fe, Co, Ni, and Cu), including key steps such as water-splitting adsorption, H activation, and hydrogen evolution, as shown in Fig. 5. The results revealed that Mn, Fe, and Cu clusters, when loaded, exhibited lower energy barriers for the hydrogen evolution step compared to the pure aTiO_2 (101) surface, thereby promoting H_2 evolution. Furthermore, Mn and Fe impeded water splitting to yield $^*H$. In contrast, the inclusion of Ni- or Co-facilitated water splitting to produce $^*H$ and activates H while discouraging the formation of H_2. Therefore, we proceeded to calculate the path for CO_2 reduction to produce C_1 on the surface of Ga_2O_3-doped TiO_2 loaded with Ni or Co metal clusters. As shown in Fig. 6, it was found that, compared with the unloaded Ga_2O_3-doped TiO_2 surface, the energy barriers for the RDS in CH_3OH and CH_4 production were significantly lowered when Ni or Co metal clusters were introduced. The impact of Ni was more significant than that of Co. In Comparison with the pure TiO_2 surface, Co could promote the formation of CH_3OH and CH_4 primarily at higher temperatures. In addition, Co loading did not enhance the production of CO, and Ni loading only made the CO's RDS energy barrier lower when the temperature gradually increased (after 200 °C), with both Ni and Co improving the selectivity of CH_3OH and CH_4. This substantiated the positive role played by the supported Ni_4 or Co_4 cluster in facilitating the direct hydrogenation and multi-electron conversion of CO_2. The electron transfer by Bader charge analysis has been investigated to further explore the possible mechanism and synergistic effect of Ga_2O_3 doping combined with Co or Ni loading on the CO_2 conversion with the H_2O reaction process. The results in Table 1 demonstrated that on

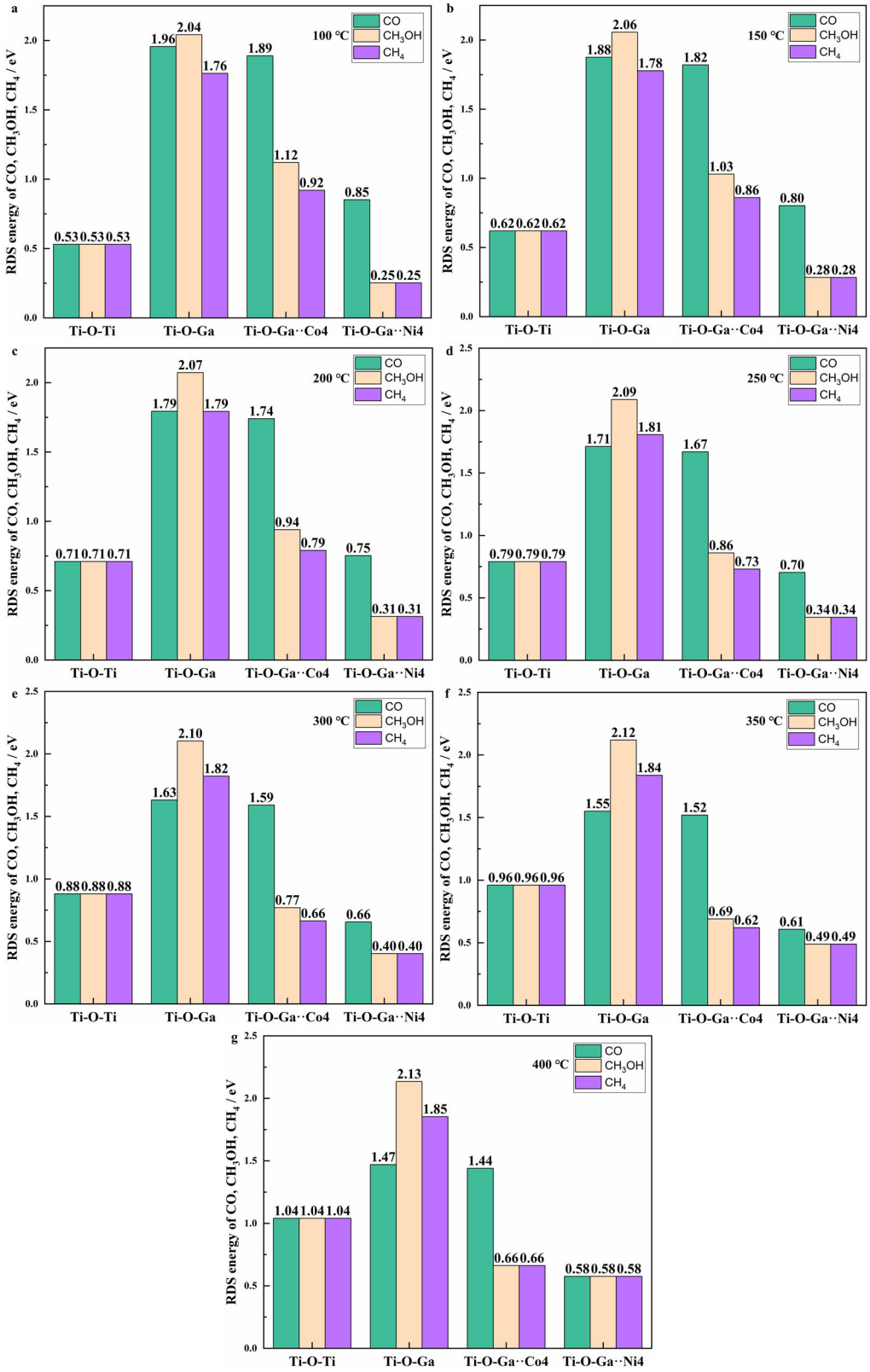

Fig. 6 | Comparison of RDS energy barriers for CO, CH_3OH, and CH_4 production on the surfaces before and after featuring bifunctional sites under different temperatures (100~400 °C). Each graph shows the RDS energy barriers of surface sites (Ti-O-Ti, Ti-O-Ga, Ti-O-Ga··Co_4, and Ti-O-Ga··Ni_4) at one specific reaction temperature: **a** 100 °C, **b** 150 °C, **c** 200 °C, **d** 250 °C, **e** 300 °C, **f** 350 °C, and **g** 400 °C.

Ti-O-Ga··Co_4 and Ti-O-Ga··Ni_4 sites, there was a decrease in positive charge on H and C atoms, while the negative charge on O atoms of CO_2 and those connected to H atoms increased. This alteration suggests an augmented electron transfer between the surface and H or CO_2, leading to an accumulation of electrons on H and CO_2 species. Consequently, the adsorption of CO_2 and H was enhanced, as shown in Supplementary Table 2. Furthermore, the longer CO_2 bond lengths signify a reduction in C=O bond energy and the weakening of the C=O bond. Based on the collective

Table 1 | The Bader charge analysis on Ti-O-Ti, Ti-O-Ga, Ti-O-Ga··Co_4, and Ti-O-Ga··Ni_4 sites after the adsorption of CO_2, H, and corresponding calculated bond lengths

Surface sites	Charge on H and O		Charge on C, O, and CO_2				Bond length/ Å
	H	O	C	O1	O2	CO_2	C=O1; C=O2
Ti-O-Ti	+0.6501	−1.1461	+2.1122	−1.0922	−1.0023	+0.0177	1.21; 1.33
Ti-O-Ga	+0.6034	−1.1201	+2.1964	−0.8620	−0.8542	+0.4802	1.27; 1.26
Ti-O-Ga··Co_4	+0.6158	−1.1517	+2.1367	−1.1224	−1.1307	−0.1164	1.28; 1.29
Ti-O-Ga··Ni_4	+0.6265	−1.1626	+2.0792	−1.1367	−1.0951	−0.1525	1.22; 1.36

computational findings, it can be inferred that Ga_2O_3 doping combined with Co or Ni loading facilitates CO_2 adsorption and the proton-donating process involved in H_2O splitting by providing additional electrons, thereby facilitating the CO_2 conversion reaction.

As the temperature rose from 100 °C to 400 °C, combined with Supplementary Fig. 8, it was observed that the reaction path on Ti-O-Ga-M_T4 site for yielding C_1 product remained constant, while the rate-determining steps underwent modifications. On the Co-loaded surface, the RDS for CO production consistently involved CO desorption, with the energy barrier decreasing as temperature increased, but was still higher compared to other surfaces. The RDS for CH_3OH production transitioned from CH_3OH desorption to '$^*HCHO \rightarrow {}^*CH_2OH$', and the energy barrier decreased with increasing temperature. For CH_4 production, the RDS shifted from '$^*CH_2OH \rightarrow {}^*CH_2$' to '$^*HCHO \rightarrow {}^*CH_2OH$'. Initially, the energy barrier decreased with rising temperature, but it subsequently began to increase at significantly high temperatures (350 °C). On the Ni-loaded surface, the RDS for CO production changed from '$^*COOH \rightarrow {}^*CO$' to CO_2 adsorption, and the energy barrier diminished as temperature increased. In contrast, the RDS for CH_3OH and CH_4 production shifted from CH_3OH desorption to '$^*HCOO \rightarrow {}^*HCOOH$' and then to CO_2 adsorption, resulting in a larger energy barrier with increasing temperature. Irrespective of temperature, the RDS energy barrier for CH_3OH and CH_4 production on the Ni-loaded surface was always lower than any other surface. The coexistence of dual sites on the surface resulted in CH_3OH and CH_4 dominating the product selectivity even at very high temperatures. In contrast to surfaces solely doped with M_2O_3, wherein only adsorption-assisted sites were introduced, on these surfaces, as temperature increased, the energy barrier for the RDS in CO production remained persistently high, like the production of CH_3OH and CH_4. Alternatively, it gradually decreased until it governed C_1 product selectivity. The dual-site configuration, combining adsorption and reduction sites, not only accelerated the multi-electron conversion of CO_2 to generate CH_3OH and CH_4 but also reduced temperature sensitivity, that is, CH_3OH and CH_4 selectivity was still very high even at very high temperatures.

In this study, how temperature affects the complex intermediate process of photothermal catalytic CO_2/H_2O reaction and C_1 product selectivity was investigated by employing periodic density functional theory methods. The surface reaction path and mechanism before and after regulating the active site were analyzed from the atomic-level perspective. It was revealed that on the pure TiO_2 semiconductor surface, the adsorption of reactants consistently emerged as the rate-determining step for C_1 production at high temperatures and that high temperatures did not favor the exothermic adsorption process. After adsorption activation, the subsequent conversion of CO_2 and H_2O on the semiconductor surface involved multiple surface intermediates and multiple hydrodeoxygenation steps, resulting in the formation of a complex reaction network and potential energy surface. To establish a more universally applicable conclusion regarding the impact of temperature on the thermodynamics of surface reactions, we introduced diverse adsorption sites by incorporating a range of metal oxides onto the TiO_2 surface. Our investigations unveiled that during the photothermal conversion of CO_2, Ti-O-M sites could always enhance CO_2 adsorption, but did not invariably promote subsequent reduction reactions. Temperature variations did not alter the overall direction of the reaction path but brought about alterations in the rate-determining step and the corresponding energy barrier for each C_1 product, thereby changing the selectivity of each C_1 product on the surface which followed the adjustment of active sites. Elevating the temperature might lead to an increased CO selectivity at the Ti-O-Ga site and a higher propensity for CH_4 and CH_3OH selectivity at the Ti-O-La site. Upon introducing bifunctional sites (Ga-O-Ti··M_T4) to facilitate adsorption and reduction, the production of CH_3OH and CH_4 could be further enhanced through the facilitation of the proton donation process of H_2O. However, it was noteworthy that as the temperature increases, it might become less favorable at the Ga-O-Ti··Ni_4 site and might favor an increased selectivity for CO. While higher temperatures could directly augment hydrocarbon product generation at the Ga-O-Ti··Co_4 site, there might be an inflection point where the rate-determining step's energy barrier started to rise. From a thermodynamic perspective, an increase in temperature did promote the reaction within a certain range, yet there might exist an optimal reaction temperature. The temperature elevation enhanced the reaction thermodynamics of C_1 product formation to varying degrees at different surface sites.

Understanding the surface thermodynamic reaction mechanism affected by temperature and the roles it plays in the adsorption and desorption of reactants, intermediates, and products should be addressed. Here, the present first-principles computational work is complementary to experimentally elucidate the processes promoted by solar-induced temperature, and might provide valuable theoretical insights to guide active site regulation and further experimental design of photothermal catalysts dedicated to the conversion of CO_2 and H_2O into hydrocarbons.

Methods

Computational methods

All calculations have been conducted in the framework of DFT[64,65] using the Perdew–Burke–Ernzerhof (PBE) functional of the generalized gradient approximation (GGA)[66] as implemented in the Vienna Ab-initio Simulation Package (VASP)[67,68]. The core-valence electron interaction was described by the project-augmented wave (PAW) pseudopotential. The empirical correction in the DFT-D3 method with Becke–Jonson damping[69] was used for long-range dispersion corrections. To balance computational accuracy and cost, the energy cutoff of 400 eV was set in the calculations, along with the convergence threshold for the self-consistent-field iteration set to 10^{-6} eV. Geometry optimizations converged when the force components were less than 0.01 eV/Å. The integration in the Brillouin zone was done on a 3 × 3 × 1 k-point grid sampled by the Gamma-centered scheme[70].

The adsorption energy of CO_2, H_2O, and H, labeled as $E_{ads\text{-}}CO_2$, $E_{ads\text{-}}H_2O$, and $E_{ads\text{-}H}$ were calculated as $E_{ads} = E(\text{total}) - E(\text{slab}) - E(\text{adsorbed substance})$. To study how temperature influences CO_2 conversion with H_2O from a thermodynamic point of view, the Gibbs free energy (ΔG) of all intermediates during the reaction were calculated based on statistical thermodynamics[71–73] by adding the importance of entropic contribution (S) and zero-point energy (ZPE) corrections as:

$$\Delta G = \Delta H - T\Delta S \quad (1)$$

$$\Delta H \approx \Delta U = \Delta E + \Delta ZPE + \Delta U_{tran} + \Delta U_{rot} + \Delta U_{vib} \quad (2)$$

$$\Delta S = \Delta S_{tran} + \Delta S_{rot} + \Delta S_{vib} \quad (3)$$

Where ΔE is the reaction energy acquired from DFT calculations of the optimized structure of reactants and products at each intermediate step, calculated as $\Delta E = E(\text{products}) - E(\text{reactants})$. ΔZPE is the difference in zero-point energy due to the reaction. ΔU and ΔS are the change in internal energy and entropy, contributed by the translation, rotation, and vibration, respectively, which could be given by:

$$U_{tran} = U_{rot} = \frac{3}{2} k_B T \quad (4)$$

$$U_{vib} = \sum_i \frac{h\nu_i}{\left(e^{h\nu_i/k_B T} - 1\right)} \quad (5)$$

$$S_{tran} = k_B \left\{ \ln\left[\left(\frac{2\pi m k_B T}{h^2} \right)^{3/2} \frac{k_B T}{P} \right] + \frac{5}{2} \right\} \quad (6)$$

$$S_{rot} = k_B \left\{ \ln\left[\frac{\sqrt{\pi I_A I_B I_C}}{\sigma} \left(\frac{8\pi^2 k_B T}{h^2} \right)^{3/2} \right] + \frac{3}{2} \right\} \quad (7)$$

$$S_{vib} = k_B \sum_i \left(\frac{h\nu_i}{k_B T\left(e^{h\nu_i/k_B T} - 1\right)} - \ln\left(1 - e^{-h\nu_i/k_B T}\right) \right) \quad (8)$$

Where T is temperature, ν_i are vibrational frequencies that could be calculated by DFT calculations. Then ΔZPE, ΔU, and ΔS are determined from ν_i associated with the normal modes of the adsorbed species calculated in the harmonic oscillator approximation, which can be calculated using VASPKIT[74] after vibration frequency calculation. The temperature (T = 298.15, 373.15, 423.15, 473.15, 523.15, 573.15, 623.15, 673.15 K) dependence of entropic and vibrational contributions to the Gibbs free energy has been explicitly taken into account. It is worth mentioning that this computational strategy for analyzing the influence of temperature effects on surface reaction mechanisms from the thermodynamics perspective has been applied to some reported research in recent years[62,75,76].

Computational models

The modified metal oxide semiconductor systems were constructed based on our previous theoretical and experimental studies[56,77,78]. Typically, TiO_2-based catalysts can maintain a stable crystal form of anatase at temperatures below approximately 450 °C. Furthermore, it has been observed that a temperature increase within this range results in a slight decrease in the band gap of TiO_2 due to the expansion of atomic spacing, though this influence is almost negligible[23]. In the meantime, taking the temperature range employed in our photothermal catalysis experiments into account, the temperature range of this study is set as 298.15~673.15 K. Consequently, the supporting catalyst, that is, the pure anatase TiO_2, whose most stable surface - (101) surface was directly introduced into the calculation. The aTiO_2(101) surface slab was optimized with three layers in a 4 × 4 supercell (144 atoms), keeping fixed the bottom layer to the bulk atomic positions and the top two layers allowed to relax. A vacuum space of 15 Å along the surface normal direction is applied to minimize unphysical interaction between periodic images and simulate the exposed surface. One bridge O atom was removed to represent the defective surface with oxygen vacancy (V_O). Furthermore, according to the reported literature, for the metal oxides (M_xO_y) decorating surface, the model of M_xO_y doped TiO_2 catalysts was built by incorporating one metal atom to replace one five-coordination Ti atom[79–81]. And as the previously extensively accepted 4-atom cluster model catalyst[73,82–84], the M_T4 cluster consists of four M_T atoms that were put onto the supporting catalyst surface, to signify the transition metal (M_T) loaded surface. The most stable adsorption configurations of all reaction intermediates at the surface reaction sites, were identified by the lowest calculated energy values among all possible configurations. The catalysts' models and the optimized reaction intermediate structures on corresponding surface-active sites can be seen in Supplementary Figs. 1 and 2, respectively.

Data availability

The authors declare that the data supporting the findings of this study are available within the article and its supplementary information files or from the corresponding authors on reasonable request.

Code availability

The VASP calculation inputs and outputs will be shared with the community upon reasonable request.

Received: 25 January 2024; Accepted: 14 June 2024;
Published online: 26 June 2024

References

1. Le, Q. V. et al. Light-driven reduction of carbon dioxide: altering the reaction pathways and designing photocatalysts toward value-added and renewable fuels. *Chem. Eng. Sci.* **237**, 116547 (2021).
2. Lin, H. et al. Toward solar-driven carbon recycling. *Joule* **6**, 294–314 (2022).
3. Hong, J. et al. Photothermal chemistry based on solar energy: from synergistic effects to practical applications. *Adv. Sci.* **9**, 2103926 (2021).
4. Li, Y. et al. Recent advances in photothermal CO_x conversion. *Sol. RRL* **6**, 2200493 (2022).
5. Wang, X. et al. Carbon nanotubes @Cu/Ni loaded BFO for photothermal catalytic conversion of CO_2 by H_2O. *Mater. Chem. Phys.* **309**, 128417 (2023).
6. Ozin, G. Accelerated optochemical engineering solutions to CO_2 photocatalysis for a sustainable future. *Matter* **5**, 2594–2614 (2022).
7. Mateo, D. et al. Fundamentals and applications of photo-thermal catalysis. *Chem. Soc. Rev.* **50**, 2173–2210 (2021).
8. Song, C. et al. Principles and applications of photothermal catalysis. *Chem. Catal.* **2**, 52–83 (2022).
9. Wang, Z. et al. A state-of-the-art review on action mechanism of photothermal catalytic reduction of CO_2 in full solar spectrum. *Chem. Eng. J.* **429**, 132322 (2022).
10. Fan, W. K. & Tahir, M. Recent developments in photothermal reactors with understanding on the role of light/heat for CO_2 hydrogenation to fuels: a review. *Chem. Eng. J.* **427**, 131617 (2022).
11. Becker, H., Ziegenbalg, D. & Güttel, R. Discriminating photochemical and photothermal effects in heterogeneous photocatalysis. *Catal. Sci. Technol.* **13**, 645–664 (2023).
12. Fang, S. & Hu, Y. H. Thermo-photo catalysis: a whole greater than the sum of its parts. *Chem. Soc. Rev.* **51**, 3609–3647 (2022).
13. Chen, Y. et al. Cooperative catalysis coupling photo-/photothermal effect to drive Sabatier reaction with unprecedented conversion and selectivity. *Joule* **5**, 3235–3251 (2021).
14. Kashyap, V. & Ghasemi, H. Solar heat localization: concept and emerging applications. *J. Mater. Chem. A* **8**, 7035–7065 (2020).
15. Rao, Z. et al. Insights into the nonthermal effects of light in dry reforming of methane to enhance the H_2/CO ratio near unity over Ni/Ga_2O_3. *ACS Catal.* **11**, 4730–4738 (2021).
16. Ning, S. et al. Microstructure induced thermodynamic and kinetic modulation to enhance CO_2 photothermal reduction: a case of atomic-scale dispersed Co-N species anchored Co@C Hybrid. *ACS Catal.* **10**, 4726–4736 (2020).
17. Liu, D. et al. Photothermally assisted photocatalytic conversion of CO_2-H_2O into fuels over a WN-WO_3 Z-scheme heterostructure. *J. Mater. Chem. A* **8**, 1077–1083 (2020).
18. Guo, R.-T. et al. Recent progress of photothermal effect on photocatalytic reduction of CO_2. *Fuel Process. Technol.* **241**, 107617 (2023).

19. Ghoussoub, M. et al. Principles of photothermal gas-phase heterogeneous CO_2 catalysis. *Energy Environ. Sci.* **12**, 1122–1142 (2019).
20. Zheng, D. et al. $LaNi_xFe_{1-x}O_3$ ($0 \le x \le 1$) as photothermal catalysts for hydrocarbon fuels production from CO_2 and H_2O. *J. Photochem. Photobiol. A* **377**, 182–189 (2019).
21. Han, B. et al. Efficient visible light photocatalytic CO_2 reforming of CH_4. *ACS Catal.* **6**, 494–497 (2016).
22. Ma, Z. et al. Temperature effects on redox potentials and implications to semiconductor photocatalysis. *Fuel* **286**, 119490 (2021).
23. Han, B. et al. A thermo-photo hybrid process for steam reforming of methane: highly efficient visible light photocatalysis. *ChemComm* **55**, 7816–7819 (2019).
24. Maarisetty, D. et al. The role of material defects in the photocatalytic CO_2 reduction: interfacial properties, thermodynamics, kinetics and mechanism. *J. CO_2 Util*. **64**, 102175 (2022).
25. Tian, J. et al. Direct conversion of CO_2 into hydrocarbon solar fuels by a synergistic photothermal catalysis. *Catalysts* **12**, 612 (2022).
26. Sun, F. et al. Concentrated full-spectrum solar-driven CO_2 reduction with H_2O to solar fuels by Au nanoparticle-decorated TiO_2. *Energy Fuels* **36**, 6433–6444 (2022).
27. Wang, K. et al. Unravelling the CC coupling in CO_2 photocatalytic reduction with H_2O on Au/TiO_{2-x}: combination of plasmonic excitation and oxygen vacancy. *Appl. Catal. B* **292**, 120147 (2021).
28. He, B. et al. Design and application of g-C_3N_4-based materials for fuels photosynthesis from CO_2 or H_2O based on reaction pathway insights. *J. Colloid Interf. Sci.* **629**, 825–846 (2023).
29. Duan, Y. et al. Simultaneous CO_2 and H_2O activation via integrated Cu single atom and N vacancy dual-site for enhanced CO photo-production. *Adv. Funct. Mater.* **33**, 2301729 (2023).
30. Fresno, F., Iglesias-Juez, A. & Coronado, J. M. Photothermal catalytic CO_2 conversion: beyond catalysis and photocatalysis. *Top. Curr. Chem.* **381**, 21 (2023).
31. Akhter, P. et al. Novel nanostructured-TiO_2 materials for the photocatalytic reduction of CO_2 greenhouse gas to hydrocarbons and syngas. *Fuel* **149**, 55–65 (2015).
32. Fu, J. et al. Product selectivity of photocatalytic CO_2 reduction reactions. *Mater. Today* **32**, 222–243 (2020).
33. Qi, Y. et al. Photoinduced defect engineering: enhanced photothermal catalytic performance of 2D black In_2O_{3-x} nanosheets with bifunctional oxygen vacancies. *Adv. Mater.* **32**, 1903915 (2020).
34. Li, X. et al. Cocatalysts for selective photoreduction of CO_2 into solar fuels. *Chem. Rev.* **119**, 3962–4179 (2019).
35. Zhang, F. et al. Photothermal catalytic CO_2 reduction over nanomaterials. *Chem. Catal.* **1**, 272–297 (2021).
36. Zhao, H., Pan, F. & Li, Y. A review on the effects of TiO_2 surface point defects on CO_2 photoreduction with H_2O. *J. Materiomics* **3**, 17–32 (2017).
37. Xu, C. & Luo, J.-L. Understanding the light-induced oxygen vacancy in the photochemical conversion. *J. Phys. Energy* **5**, 011001 (2023).
38. Zhang, Y. et al. Atomic-level reactive sites for semiconductor-based photocatalytic CO_2 reduction. *Adv. Energy Mater.* **10**, 1903879 (2020).
39. Nguyen, T. P. et al. Recent advances in TiO_2-based photocatalysts for reduction of CO_2 to fuels. *Nanomaterials* **10**, 337 (2020).
40. Bian, J. et al. Strategies and reaction systems for solar-driven CO_2 reduction by water. *Carbon Neutr.* **1**, 5 (2022).
41. Torres, J. A. et al. Enhancing TiO_2 activity for CO_2 photoreduction through MgO decoration. *J. CO2 Util.* **35**, 106–114 (2020).
42. Kwon, S. et al. Alkaline-earth metal-oxide overlayers on TiO_2: application toward CO_2 photoreduction. *Catal. Sci. Technol.* **6**, 7885–7895 (2016).
43. Ullah, S. et al. Photoenhanced CO_2 methanation over La_2O_3 promoted Co/TiO_2 catalysts. *Appl. Catal. B* **294**, 120248 (2021).
44. Liu, H. et al. Effect of CeO_2 addition on Ni/Al_2O_3 catalysts for methanation of carbon dioxide with hydrogen. *J. Nat. Gas. Chem.* **21**, 703–707 (2012).
45. Huang, Z. et al. CO_2 capture, storage, and conversion using a praseodymium-modified Ga_2O_3 photocatalyst. *J. Mater. Chem. A* **5**, 19351–19357 (2017).
46. Bansode, A. & Urakawa, A. Towards full one-pass conversion of carbon dioxide to methanol and methanol-derived products. *J. Catal.* **309**, 66–70 (2014).
47. Akatsuka, M. et al. Preparation of Ga_2O_3 photocatalyst highly active for CO_2 reduction with water without cocatalyst. *Appl. Catal. B* **262**, 118247 (2020).
48. Dang, S. et al. Role of zirconium in direct CO_2 hydrogenation to lower olefins on oxide/zeolite bifunctional catalysts. *J. Catal.* **364**, 382–393 (2018).
49. Wei, S. et al. Improved photocatalytic CO_2 conversion efficiency on Ag loaded porous Ta_2O_5. *Appl. Surf. Sci.* **563**, 150273 (2021).
50. Li, X. et al. Enhanced electroreduction of CO_2 to C_{2+} products on heterostructured Cu/oxide electrodes. *Chem* **8**, 2148–2162 (2022).
51. Deng, Y. et al. Solar-energy-driven photothermal catalytic C-C coupling from CO_2 reduction over WO_{3-x}. *Chin. J. Catal.* **43**, 1230–1237 (2022).
52. Lee, J. H. et al. Cost-effective and dynamic carbon dioxide conversion into methane using a $CaTiO_3$@Ni-Pt catalyst in a photo-thermal hybrid system. *J. Photochem. Photobiol. A* **364**, 219–232 (2018).
53. Meng, X. et al. Photothermal conversion of CO_2 into CH_4 with H_2 over Group VIII nanocatalysts: an alternative approach for solar fuel production. *Angew. Chem. Int. Ed.* **53**, 11478–11482 (2014).
54. He, Z.-H. et al. Photothermal CO_2 hydrogenation to hydrocarbons over trimetallic Co-Cu-Mn catalysts. *Green Chem.* **23**, 5775–5785 (2021).
55. Pannwitz, A. & Wenger, O. S. Proton-coupled multi-electron transfer and its relevance for artificial photosynthesis and photoredox catalysis. *ChemComm* **55**, 4004–4014 (2019).
56. Zhang, L. et al. Elaborated reaction pathway of photothermal catalytic CO_2 conversion with H_2O on gallium oxide-decorated and -defective surfaces. *Chem. Eur. J.* **28**, e202104490 (2022).
57. Vu, N.-N., Kaliaguine, S. & Do, T.-O. Critical aspects and recent advances in structural engineering of photocatalysts for sunlight-driven photocatalytic reduction of CO_2 into fuels. *Adv. Funct. Mater.* **29**, 1901825 (2019).
58. Wang, F., Di Valentin, C. & Pacchioni, G. Doping of WO_3 for photocatalytic water splitting: hints from density functional theory. *J. Phys. Chem. C* **116**, 8901–8909 (2012).
59. Li, Z. et al. Photo-driven hydrogen production from methanol and water using plasmonic Cu nanoparticles derived from layered double hydroxides. *Adv. Funct. Mater.* **33**, 2213672 (2023).
60. Yang, S. et al. Mechanism of transition metal cluster catalysts for hydrogen evolution reaction. *Int. J. Hydrog. Energy* **46**, 3484–3492 (2021).
61. Zhao, J. et al. Plasmonic Cu nanoparticles for the low-temperature photo-driven water-gas shift reaction. *Angew. Chem. Int. Ed.* **62**, e202219299 (2023).
62. Zhang, X. et al. Photothermal catalytic water splitting at diverse two-phase interfaces based on Cu-TiO_2. *ACS Appl. Energy Mater.* **5**, 4564–4576 (2022).
63. Zhang, L. et al. Synergistic modulation between non-thermal and thermal effects in photothermal catalysis based on modified In_2O_3. *ACS Appl. Mater. Interfaces* **15**, 39304–39318 (2023).
64. Hohenberg, P. & Kohn, W. Inhomogeneous electron gas. *Phys. Rev.* **136**, B864–B871 (1964).
65. Kohn, W. & Sham, L. J. Self-consistent equations including exchange and correlation effects. *Phys. Rev.* **140**, A1133–A1138 (1965).
66. Perdew, J. P., Burke, K. & Ernzerhof, M. Generalized gradient approximation made simple. *Phys. Rev. Lett.* **77**, 3865–3868 (1996).

67. Kresse, G. & Furthmüller, J. Efficiency of ab-initio total energy calculations for metals and semiconductors using a plane-wave basis set. *Comput. Mater. Sci.* **6**, 15–50 (1996).
68. Kresse, G. & Furthmüller, J. Efficient iterative schemes for ab initio total-energy calculations using a plane-wave basis set. *Phys. Rev. B* **54**, 11169–11186 (1996).
69. Grimme, S. et al. A consistent and accurate ab initio parametrization of density functional dispersion correction (DFT-D) for the 94 elements H-Pu. *J. Chem. Phys.* **132**, 154104 (2010).
70. Setyawan, W. & Curtarolo, S. High-throughput electronic band structure calculations: challenges and tools. *Comput. Mater. Sci.* **49**, 299–312 (2010).
71. Xu, Y. & Shelton, W. O_2 reduction by lithium on Au(111) and Pt(111). *J. Chem. Phys.* **133**, 024703 (2010).
72. Psofogiannakis, G., St-Amant, A. & Ternan, M. Methane oxidation mechanism on Pt(111): a cluster model DFT study. *J. Phys. Chem. B* **110**, 24593–24605 (2006).
73. Shen, C. et al. Synergistic effect of the metal-support interaction and interfacial oxygen vacancy for CO_2 hydrogenation to methanol over Ni/In_2O_3 catalyst: a theoretical study. *J. Energy Chem.* **65**, 623–629 (2022).
74. Wang, V. et al. VASPKIT: a user-friendly interface facilitating high-throughput computing and analysis using VASP code. *Comput. Phys. Commun.* **267**, 108033 (2021).
75. Guo, S. et al. Boosting photocatalytic hydrogen production from water by photothermally induced biphase systems. *Nat. Commun.* **12**, 1343 (2021).
76. Zhu, X. et al. Boosting solar photothermal synergy for efficient overall water splitting based on Mg, Al codoped and Rh/Cr_2O_3/CoOOH coloaded $SrTiO_3$. *Chem. Eng. J.* **479**, 147636 (2024).
77. Xu, C. et al. Photothermal coupling factor achieving CO_2 reduction based on palladium-nanoparticle-loaded TiO_2. *ACS Catal.* **8**, 6582–6593 (2018).
78. Xu, C. et al. Guiding effective nanostructure design for photo-thermochemical CO_2 conversion: from DFT calculations to experimental verifications. *Nano Energy* **41**, 308–319 (2017).
79. Dou, M. et al. Mechanistic insight into the modification of the surface stability of In_2O_3 catalyst through metal oxide doping. *Catal. Lett.* **148**, 3723–3731 (2018).
80. Zhang, M., Dou, M. & Yu, Y. Theoretical study of the promotional effect of ZrO_2 on In_2O_3 catalyzed methanol synthesis from CO_2 hydrogenation. *Appl. Surf. Sci.* **433**, 780–789 (2018).
81. Jiang, X. et al. A combined experimental and DFT study of H_2O effect on In_2O_3/ZrO_2 catalyst for CO_2 hydrogenation to methanol. *J. Catal.* **383**, 283–296 (2020).
82. Li, M.-R., Lu, Z. & Wang, G.-C. The effect of potassium on steam-methane reforming on the Ni_4/Al_2O_3 surface: a DFT study. *Catal. Sci. Technol.* **7**, 3613–3625 (2017).
83. Sihag, A. et al. DFT insights into comparative hydrogen adsorption and hydrogen spillover mechanisms of Pt4/Graphene and Pt4/Anatase (101) surfaces. *J. Phys. Chem. C* **123**, 25618–25627 (2019).
84. Li, Y. et al. Photo-assisted CO/CO_2 methanation over Ni/TiO_2 catalyst: experiment and density functional theory calculation. *ChemCatChem* **14**, e202200182 (2022).

Acknowledgements

This work was financially supported by the National Natural Science Foundation of China (52341602), Zhejiang Provincial Natural Science Foundation of China under Grant No. LDT23E06014E06, Zhejiang Provincial Natural Science Foundation of China under Grant No. LQ24E060001, National Key Research and Development Project (2023YFC3710800), Fundamental Research Funds for the Central Universities (2022ZFJH004), and funded by the China Scholarship Council.

Author contributions

L.Z.: Conceptualization; methodology; validation; formal analysis; investigation; writing original draft; visualization. C.-Q. L.: Methodology; investigation. Y.L.: Formal analysis; investigation. C.-Y. X.: Revision; feedback; editing. Y.-W. Z.: Resources; project administration; funding acquisition. All authors have given approval to the final version of the manuscript.

Competing interests

The authors declare no competing interests.

Additional information

Supplementary information The online version contains supplementary material available at https://doi.org/10.1038/s41524-024-01325-3.

Correspondence and requests for materials should be addressed to Chenyu Xu or Yanwei Zhang.